Intrinsic nonlinear Hall effect in two-dimensional honeycomb topological antiferromagnets

Zheng-Yang Zhuang and Zhongbo Yan*
Guangdong Provincial Key Laboratory of Magnetoelectric Physics and Devices, State Key Laboratory of Optoelectronic Materials and Technologies, and School of Physics, Sun Yat-sen University, Guangzhou 510275, China

(Received 5 February 2024; revised 27 April 2024; accepted 20 May 2024; published 30 May 2024)

Two-dimensional systems with honeycomb lattice are known to be a paradigmatic platform to explore the various types of Hall effects, owing to that the interplay of lattice geometry, spin-orbit coupling and magnetism can give rise to very rich features in the quantum geometry of wave functions. In this work, we consider honeycomb topological antiferromagets that are effectively described by a $\mathcal{PT}$-symmetric antiferromagnetic Kane-Mele model, and explore the evolution of its nonlinear Hall response with respect to the change of lattice anisotropy, chemical potential, and the direction of the Néel vector. Due to the $\mathcal{PT}$-symmetry, the leading-order Hall effect of quantum geometric origin is the time-reversal-odd intrinsic nonlinear Hall effect, which is a second-order effect of electric fields and is independent of the scattering time. We investigate the behavior of the intrinsic nonlinear Hall conductivity tensor across topological phase transitions driven by antiferromagnetic exchange field and lattice anisotropy and find that its components do not change sign, which is different from the time-reversal-even nonlinear Hall effect of Berry curvature dipole origin. In the weakly doped regime, we find that the intrinsic nonlinear Hall effect is valley polarized. By varying the chemical potential, we find that the nonlinear Hall conductivity tensors exhibit kinks when the Fermi surface undergoes Lifshitz transitions. Furthermore, we find that the existence of spin-orbit coupling to lift the spin-rotation symmetry is decisive for the use of intrinsic nonlinear Hall effect to detect the direction of the Néel vector. Our work shows that the two-dimensional honeycomb topological antiferromagnets are an ideal class of material systems with rich properties for the study of intrinsic nonlinear Hall effect.

DOI: 10.1103/PhysRevB.109.174443

I. INTRODUCTION

The quantum geometry of wave functions has a fundamental and deep connection with the behavior of electrons. Two basic quantum geometric quantities are the quantum metric and Berry curvature, which correspond to the real part and imaginary part of the so-called quantum geometric tensor [1], respectively. The Berry curvature has been extensively studied over the past few decades and revealed to be an indispensable factor to understand many important phenomena in materials, with the most celebrated example being its application in understanding the quantized (anomalous) Hall effect [2,3] and the generic nonquantized anomalous Hall effect in magnetic metals [4] or topological semimetals [5]. Compared to the Berry curvature, the quantum metric started to attract wide interest in the condensed-matter field much more lately. The reason is partly due to that the quantum metric influences the electrons relatively more subtly, unlike the Berry curvature that gives a transparent contribution to the velocity operator [6]. Nevertheless, recent studies have shown that the quantum metric is also fundamentally important for the understanding of many important phenomena, such as the superconductivity in flat bands [7–12], optical responses [13–15], etc. [16].

In the past few years, the generalized higher-order moments of Berry curvature and quantum metric have further generated considerable interest as they can induce Hall-type effects in the nonlinear response regime [17–59]. The two nonlinear Hall effects (NLHEs) that have attracted particular interest are the time-reversal-even NLHE of Berry-curvature-dipole origin [19] (for the convenience of discussion, we dub it as Berry-curvature-dipole NLHE) and the time-reversal-odd NLHE of quantum-metric-dipole (or say Berry connection polarizability) origin [18] (known as intrinsic NLHE) in inversion-asymmetric systems. Because of the fundamental difference under time reversal, the Berry-curvature-dipole NLHE can appear in a time-reversal invariant system, whereas the intrinsic NLHE can only show up in systems without time-reversal symmetry. The adjective "intrinsic" refers to the fact that the effect does not depend on the scattering time and only depends on the band property. Being a time-reversal odd effect, the intrinsic NLHE has been shown in theory that it holds promise for applications in antiferromagnetic spintronics as it has the power to detect one key property of the antiferromagnets, the Néel vector [60,61]. Besides the prospect of applications in spintronics, the detection of the direction of the Néel vector is also of significant importance in its own right, since many properties of an antiferromagnet, such as band topology [62,63], sensitively depend on it. Remarkably, the intrinsic NLHE and its sign change upon reversing the

*yanzhb5@mail.sysu.edu.cn

Néel vector have recently been experimentally observed in even-layered topological antiferromagnets [64,65], $MnBi_2Te_4$. This breakthrough has paved the way to explore the interplay of antiferromagnetism and other factors of a system through the intrinsic NLHE in experiment.

The lattice structure, spin-orbit coupling, and magnetism are three factors that strongly influence the band structure and the quantum geometry of the Bloch wave functions. When the band structure sensitively depends on their interplay, it is natural to expect that the intrinsic NLHE would exhibit characteristic features. Among various lattice structures, the two-dimensional (2D) honeycomb lattice is known to be a paradigmatic platform where the spin-orbit coupling and magnetism can influence the band topology in a nontrivial way [66–68]. Therefore, a honeycomb topological antiferromagnet is expected to be an ideal platform to explore the intrinsic NLHE [45]. With this picture in mind, in this work we consider honeycomb topological antiferromagets effectively described by a $\mathcal{PT}$-symmetric antiferromagnetic Kane-Mele model and explore the evolution of the intrinsic NLHE with respect to the change of lattice anisotropy, band topology, chemical potential, and the direction of the Néel vector. Our main findings include: (i) the lattice anisotropy breaking the $\mathcal{C}_{3z}$ rotation symmetry is crucial for having a nonzero intrinsic NLHE; (ii) when the band topology changes from a quantum spin Hall insulator to a trivial insulator or a boundary-obstructed atomic insulator, the intrinsic NLHE preserves its direction, which is distinct from the Berry-curvature-dipole NLHE; (iii) the intrinsic NLHE is valley-polarized in the weakly doped regime and exhibit nonanalyticity when the Fermi surface undergoes Lifshitz transitions; (iv) the existence of spin-orbit coupling to lift the spin-rotation symmetry is decisive for detecting the direction of the Néel vector. These results suggest that the intrinsic NLHE provides an effective tool to measure basic properties of 2D honeycomb topological antiferromagnets.

The paper is organized as follows. In Sec. II, we show the effective tight-binding Hamiltonian and discuss the important symmetries and possible topological phases associated with the Hamiltonian. In Sec. III, we investigate the behavior of the intrinsic NLHE across two types of topological phase transitions. In Sec. IV, we study the dependence of the intrinsic NLHE on the chemical potential and the direction of the Néel vector. In Sec.V, we discuss our findings and conclude the paper.

II. THEORETICAL MODEL

A $\mathcal{PT}$-symmetric honeycomb collinear antiferromagnet with finite intrinsic spin-orbit coupling can be effectively described by the tight-binding Kane-Mele model. The Hamiltonian is given by $H = \sum_{\boldsymbol{k}} \Psi_{\boldsymbol{k}}^\dagger \mathcal{H}(\boldsymbol{k}) \Psi_{\boldsymbol{k}}$, where the basis is chosen as $\Psi_{\boldsymbol{k}}^\dagger = (c_{A,\uparrow,\boldsymbol{k}}^\dagger, c_{B,\uparrow,\boldsymbol{k}}^\dagger, c_{A,\downarrow,\boldsymbol{k}}^\dagger, c_{B,\downarrow,\boldsymbol{k}}^\dagger)$ and the momentum-space Hamiltonian reads [69,70]

$$\mathcal{H}(\boldsymbol{k}) = \sum_{i=1}^{3} t_i [\cos(\boldsymbol{k}\cdot\boldsymbol{a}_i) s_0\sigma_x + \sin(\boldsymbol{k}\cdot\boldsymbol{a}_i) s_0\sigma_y] + 2\lambda_{\rm so} \sum_i \sin(\boldsymbol{k}\cdot\boldsymbol{b}_i) s_z\sigma_z + (\boldsymbol{M}\cdot\boldsymbol{s})\sigma_z. \quad (1)$$

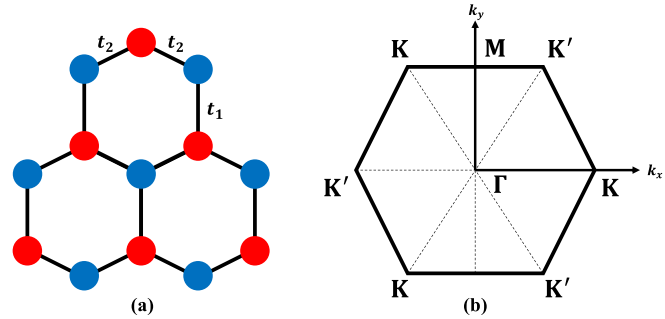

FIG. 1. (a) Schematic diagram of the honeycomb lattice with a specific type of lattice anisotropy that preserves the mirror symmetry about the xz plane. Blue and red dots refer to A and B sublattices, respectively. (b) The Brillouin zone and some high-symmetric points.

The first line describes the nearest-neighbor hoppings, the first term in the second line represents the intrinsic spin-orbit coupling involving next-nearest-neighbor hoppings, and the last term denotes the exchange field associated with the antiferromagnetic order. $(s_0; s_x, s_y, s_z)$ and $(\sigma_0; \sigma_x, \sigma_y, \sigma_z)$ are the identity matrix and Pauli matrices in the spin and sublattice subspaces, respectively. The three nearest-neighbor lattice vectors are given by $\boldsymbol{a}_1 = a(0, 1)$, $\boldsymbol{a}_2 = \frac{a}{2}(\sqrt{3}, -1)$, $\boldsymbol{a}_3 = \frac{a}{2}(-\sqrt{3}, -1)$, and the three next-nearest-neighbor lattice vectors are determined by $\boldsymbol{a}_i$ through the relation: $\boldsymbol{b}_1 = \boldsymbol{a}_2 - \boldsymbol{a}_3$, $\boldsymbol{b}_2 = \boldsymbol{a}_3 - \boldsymbol{a}_1$ and $\boldsymbol{b}_3 = \boldsymbol{a}_1 - \boldsymbol{a}_2$. For notational simplicity, we set the lattice constant $a = 1$ throughout.

Due to the antiferromagnetic exchange field, the above Hamiltonian does not have the spinful time-reversal symmetry (symmetry operator is $\mathcal{T} = -is_y\sigma_0\mathcal{K}$ with $\mathcal{K}$ the complex conjugate operator) and inversion symmetry ($\mathcal{P} = s_0\sigma_x$). However, the Hamiltonian has their combination, the spinful $\mathcal{PT}$ symmetry. The symmetry operator is $\mathcal{PT} = -is_y\sigma_x\mathcal{K}$, where $\mathcal{K}$ denotes the complex conjugate operator and the symmetry operator satisfies $(\mathcal{PT})^2 = -1$. This combinational symmetry on one hand enforces the band to be doubly degenerate, and on the other hand makes the Berry curvature identically vanishing. As a result, any Hall-type effect with a Berry-curvature origin is expected to vanish. When the Néel vector is aligned in the z direction and the hopping constants are isotropic, the Hamiltonian also contains several important crystallographic symmetries that could have a strong impact on the band topology and intrinsic NLHE, including the $\mathcal{C}_{3z}$ rotation symmetry ($\mathcal{C}_{3z} = e^{i\frac{\pi}{3}s_z\sigma_0}$), and the mirror symmetries about the xy ($\mathcal{M}_z = is_z\sigma_0$) and xz ($\mathcal{M}_y = is_y\sigma_x$) planes. To be general, we incorporate lattice anisotropy that can be caused by intrinsic lattice corrugation or extrinsic strain, and assume that the Néel vector can point to any direction. To be specific, for the lattice anisotropy, we set $t_3 = t_2$, but allow these two hopping constants to be different from t_1, as illustrated in Fig. 1. For this type of lattice anisotropy, the $\mathcal{C}_{3z}$ rotation symmetry is broken once $t_1 \neq t_2$, but the mirror symmetry about the xz plane remains. For the convenience of discussion, we introduce the ratio $\eta = t_1/t_2$ to characterize the extent of lattice anisotropy. The more η deviates from 1, the stronger the lattice anisotropy is.

The band topology of the Hamiltonian in Eq. (1) sensitively depends on the spin-orbit coupling and antiferromagnetic

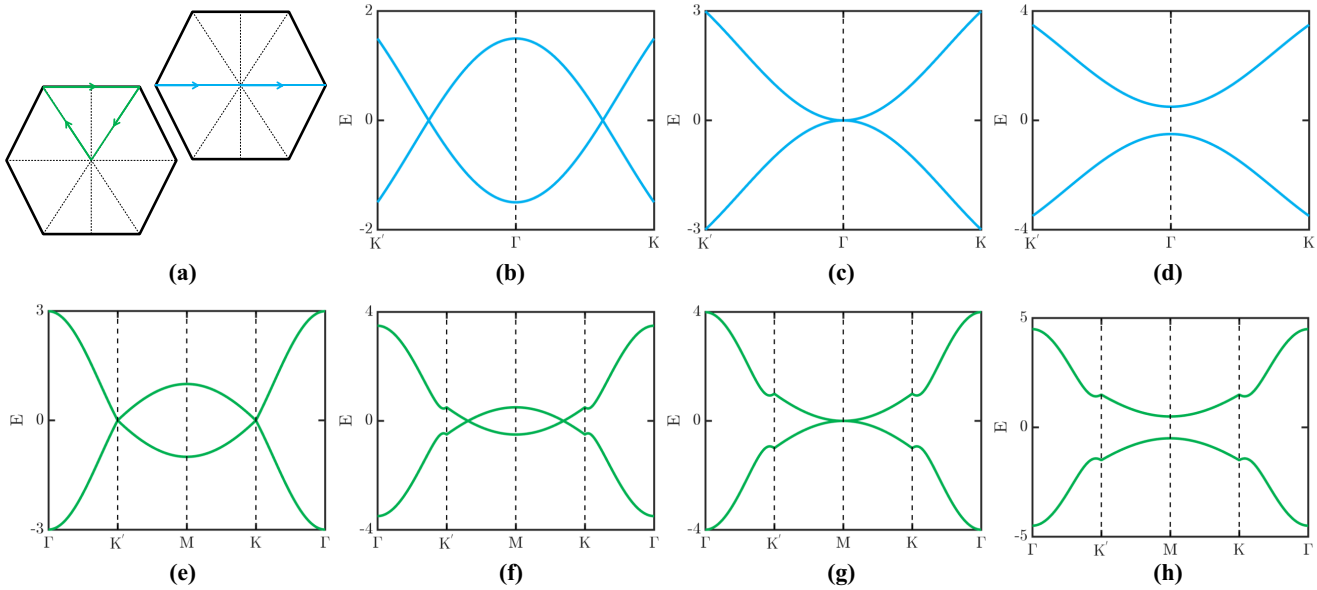

FIG. 2. The evolution of energy spectra along different paths in the Brillouin zone across the topological phase transition from a Dirac semimetal to an insulator. The light blue and green lines in (a) represent two different paths, with their corresponding energy spectra plotted in (b)–(d) and (e)–(h), respectively. When $\eta = 1$, two Dirac cones are located at the two valleys **K** and **K**′. As η deviates from 1, the two Dirac points move away from the two valleys and eventually merge at the high symmetry point **Γ** ($\eta = -2$) or **M** ($\eta = 2$), leading to the opening of the bulk energy gap once $|\eta| > 2$. In (b)–(h), the values for η are given as -0.5, -2, -2.5, 1, 1.5, 2, and 2.5. The shared parameters are given by $t_2 = 1$, $\lambda_{so} = 0$, and $M_x = M_y = M_z = 0$.

exchange field. Without the spin-orbit coupling and antiferromagnetic exchange field, it is known that the Hamiltonian realizes a Dirac semimetal with two Dirac points at the two valleys, **K** and **K**′, for the case without lattice anisotropy [71]. Weak lattice anisotropy shifts the locations of the two Dirac points, but cannot annihilate them due to the protection of a spinless $\mathcal{PT}$ symmetry (the corresponding symmetry operator is $\mathcal{PT} = s_0\sigma_x\mathcal{K}$, satisfying $(\mathcal{PT})^2 = 1$). When the lattice anisotropy reaches a critical condition ($\eta = \pm 2$), the two Dirac points converge and annihilate, and a further increase of the lattice anisotropy opens an energy gap and drives the system to an insulator [72], as illustrated in Fig. 2.

As long as the lattice anisotropy does not annihilate the two Dirac points, the presence of spin-orbit coupling will immediately gap out the Dirac points due to a lifting of the spinless $\mathcal{PT}$ symmetry, accompanying with a direct transition from the Dirac semimetal to a quantum spin Hall insulator with helical edge states [69,70], as illustrated in Fig. 3(a). Interestingly, recent works have shown that if the lattice anisotropy is strong, the quantum spin Hall insulator does not become a featureless trivial insulator, instead, it will evolve to a boundary-obstructed atomic insulator which supports boundary floating bands or corner states for appropriate geometry [73,74], as illustrated in Fig. 3(b).

In the quantum spin Hall regime, when the antiferromagnetic exchange field is also brought in, the time-reversal symmetry protecting the helical edge states is broken. Nevertheless, the helical edge states can remain stable if the Néel vector is in the z direction and the strength of the exchange field is lower than a critical value ($M_c = 3\sqrt{3}\lambda_{so}$ for the isotropic-hopping case), as illustrated in Figs. 3(c) and 3(d). There are two ways to understand the robustness of the helical edge states. The first one is that the spin remains a good quantum number for this special case, therefore, the Hamiltonian remains to be characterized by spin Chern number [75]. To be concrete, as $[s_z, \mathcal{H}(\boldsymbol{k})] = 0$, the Hamiltonian (1) can be decomposed as the direct sum of two independent parts

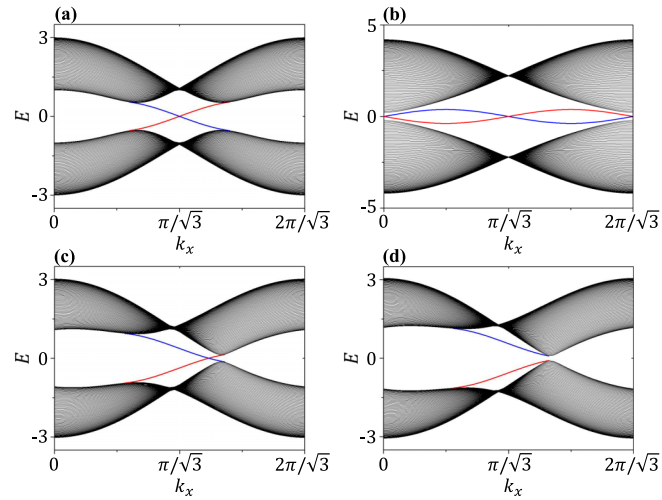

FIG. 3. (a) Quantum spin Hall insulator with a pair of helical edge states. (b) Boundary-obstructed atomic insulator with boundary floating bands driven by lattice anisotropy. (c) The quantum spin Hall insulator remains stable when the antiferromagnetic exchange field is below the critical value. (d) The quantum spin Hall insulator is transited to a trivial insulator when the antiferromagnetic exchange field is beyond the critical value. For all figures, $t_2 = 1$, $\lambda_{so} = 0.1$, $M_x = M_y = 0$ and the number of unit cells $N_y = 100$. In (a), $\eta = 1$ and $M_z = 0$; In (b), $\eta = 2.2$, and $M_z = 0$; In (c), $\eta = 1$ and $M_z = 0.4$; In (d), $\eta = 1$ and $M_z = 0.6$.

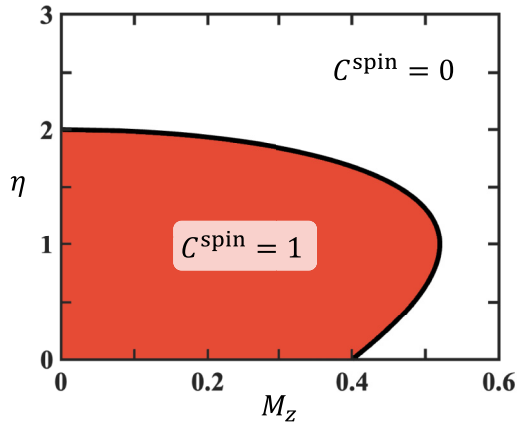

FIG. 4. The phase diagram with respect to η and M_z. Parameters are $t_2 = t_3 = 1$, $\lambda_{\text{so}} = 0.1$ and $M_x = M_y = 0$. In the region with $C^{\text{spin}} = 1$, the system is a quantum spin Hall insulator with a pair of helical edge states.

in accordance with the two eigenvalues of s_z, i.e., $\mathcal{H}(\boldsymbol{k}) = \mathcal{H}_{s_z=1}(\boldsymbol{k}) \oplus \mathcal{H}_{s_z=-1}(\boldsymbol{k})$, where

$$\mathcal{H}_{s_z=s}(\boldsymbol{k}) = \sum_{i=1}^{3} t_i[\cos(\boldsymbol{k}\cdot\boldsymbol{a}_i)\sigma_x + \sin(\boldsymbol{k}\cdot\boldsymbol{a}_i)\sigma_y] + s\left[2\lambda_{\text{so}}\sum_{i=1}^{3}\sin(\boldsymbol{k}\cdot\boldsymbol{b}_i) + M_z\right]\sigma_z \tag{2}$$

with $s = \pm 1$. The two-band Hamiltonians can be expressed as the form: $\boldsymbol{d}^s(\boldsymbol{k})\cdot\boldsymbol{\sigma}$, with the three components of $\boldsymbol{d}^s(\boldsymbol{k})$ being the coefficients before the corresponding Pauli matrices. For each spin sector, the Hamiltonian lacks time-reversal symmetry and is hence characterized by the Chern number,

$$C_s = \frac{1}{4\pi}\int_{\text{BZ}} dk_x dk_y \frac{\boldsymbol{d}^s(\boldsymbol{k})\cdot\left[\partial_{k_x}\boldsymbol{d}^s(\boldsymbol{k})\times\partial_{k_y}\boldsymbol{d}^s(\boldsymbol{k})\right]}{|\boldsymbol{d}^s(\boldsymbol{k})|^3}. \tag{3}$$

As the two spin sectors are related by time-reversal symmetry, one has $C_{+1} = -C_{-1}$. While the total Chern number defined as $C_T = C_{+1} + C_{-1}$ is forced to be zero, the spin Chern number, which is defined as $C^{\text{spin}} = (C_{+1} - C_{-1})/2$ [75], can be nonzero. The spin Chern number counts the number of pairs of helical edge states. It will not change its nontrivial value unless the bulk energy gap closes when the antiferromagnetic exchange field reaches its critical value, as illustrated by the phase diagram shown in Fig. 4. The second one is that the the Hamiltonian has the mirror symmetry about the xy plane (recall $\mathcal{M}_z = is_z\sigma_0$) for this special case. This mirror symmetry can also protect the helical edge states as a mirror Chern number can be defined to characterize the Hamiltonian [76]. For this Hamiltonian, the mirror Chern number is just equal to the spin Chern number, as the two different mirror-sector Hamiltonians obtained by decomposing the Hamiltonian in accordance with the two opposite eigenvalues of $\mathcal{M}_z$ are exactly the same as the two spin-sector Hamiltonians given in Eq. (2). In other words, the topological gapped phase can be equivalently interpreted as either a quantum spin Hall insulator or a topological mirror insulator.

Once the direction of the Néel vector deviates away from the z direction, the $\mathcal{M}_z$ mirror symmetry is broken and the spin is also no longer a conserved quantity. As a result, the helical edge states will immediately be gapped due to the lack of any symmetry protection. Commonly, the opening of a gap to the edge states suggests that the resulting phase becomes a trivial insulator. However, the trivialness is only strict in the first-order topology. The resulting phase without gapless edge states is in fact not completely topologically trivial. In Ref. [77], the authors showed that, if the honeycomb lattice consists of two parts with opposite in-plane Néel vectors, despite the absence of gapless edge states in each part, 0D topological bound states will emerge at the ends of their interface. All of these results reflect that the quantum geometric properties of honeycomb-lattice materials have a sensitive dependence on the interplay of lattice anisotropy, spin-orbit coupling, and antiferromagnetism.

III. INTRINSIC NLHE ACROSS TOPOLOGICAL PHASE TRANSITIONS

As discussed above, when the Néel vector is aligned in the z direction, the system will undergo a topological phase transition from a quantum spin Hall insulator to a trivial insulator with the increase of the antiferromagnetic exchange field, or to a boundary-obstructed atomic insulator with the increase of lattice anisotropy. In the following, we explore the behavior of the intrinsic NLHE across these two types of topological phase transitions.

Before start, we first give a brief review of the intrinsic NLHE. In 2014, Gao, Yang and Niu showed that the electric field can induce a first-order correction to the Berry curvature [18]. As a result, a second-harmonic Hall-type current can arise. The Hall-type current is of the form $j^{\text{int}}_\alpha = \chi^{\text{int}}_{\alpha\beta\gamma}\mathcal{E}^\beta\mathcal{E}^\gamma$, where $\mathcal{E}^\beta$ represents the electric-field component in the β direction, and $\chi^{\text{int}}_{\alpha\beta\gamma}$ is a conductivity tensor independent of scattering time. The explicit expression of $\chi^{\text{int}}_{\alpha\beta\gamma}$ is given by [18,60,61]

$$\chi^{\text{int}}_{\alpha\beta\gamma} = e^3\sum_n\int\frac{d^Dk}{(2\pi)^D}\Lambda_{\alpha\beta\gamma}(\boldsymbol{k})\frac{\partial f(E_n)}{\partial E_n}, \tag{4}$$

where D is the dimension, n is the band index, and $f(E_n)$ is the equilibrium Fermi-Dirac distribution function of the nth band. The tensor $\Lambda_{\alpha\beta\gamma}(\boldsymbol{k})$ is given by

$$\Lambda^{(n)}_{\alpha\beta\gamma}(\boldsymbol{k}) = v^{(n)}_\alpha(\boldsymbol{k})G^{(n)}_{\beta\gamma}(\boldsymbol{k}) - v^{(n)}_\beta(\boldsymbol{k})G^{(n)}_{\alpha\gamma}(\boldsymbol{k}), \tag{5}$$

where $v^{(n)}_\alpha = \partial E_n/\partial k_\alpha$ is the group velocity of the nth band, and $G^{(n)}_{\beta\gamma}$ is of the form [18,60,61]

$$G^{(n)}_{\beta\gamma}(\boldsymbol{k}) = 2\text{Re}\sum_{m\neq n}\frac{A_{nm,\beta}(\boldsymbol{k})A_{mn,\gamma}(\boldsymbol{k})}{E_n(\boldsymbol{k}) - E_m(\boldsymbol{k})}. \tag{6}$$

Above $A_{nm,\beta}(\boldsymbol{k}) = i\langle u_n(\boldsymbol{k})|\partial_{k_\beta}u_m(\boldsymbol{k})\rangle$ with $n \neq m$ is the interband Berry connection. It is noteworthy that $\text{Re}\sum_{m\neq n}A_{nm,\beta}(\boldsymbol{k})A_{mn,\gamma}(\boldsymbol{k})$ corresponds to the quantum metric of the nth band, suggesting the quantum metric origin of this second-order response. In Eq. (4), the derivative of the Fermi-Dirac distribution function indicates that this effect is a Fermi-surface property. From Eq. (5), it is easy

to see that the tensor $\Lambda^{(n)}_{\alpha\beta\gamma}$, and so the conductivity tensor $\chi^{\rm int}_{\alpha\beta\gamma}$, is antisymmetric about the first two subscripts, i.e., $\chi^{\rm int}_{\alpha\beta\gamma} = -\chi^{\rm int}_{\beta\alpha\gamma}$, suggesting that the resulting current is a Hall-like current. Because of this property, the conductivity tensor only have two independent components in 2D, including $\chi^{\rm int}_{xyx}$ and $\chi^{\rm int}_{xyy}$. On the other hand, the energy difference between bands in the denominator of Eq. (6) implies that $G^{(n)}_{\beta\gamma}$ should be prominent near the band edge, and a decrease in the band energy gap could benefit the enhancement of this effect. Therefore, when the system is close to a topological phase transition, the intrinsic NLHE is expected to be prominent.

Let us first focus on the topological phase transition driven by the z-directional antiferromagnetic exchange field. To simplify the discussion, we consider the lattice anisotropy to be weak for this case. Accordingly, the band edge will be located near one of the two valleys when the system is close to the topological phase transition. By an expansion of the bulk Hamiltonian around the two valleys and only keeping the leading-order terms, we find that the corresponding low-energy Hamiltonians are given by

$$\mathcal{H}_\chi(\boldsymbol{q}) = -\chi\frac{3t_2}{2}q_x\sigma_x + \left(t_1+\frac{t_2}{2}\right)q_y\sigma_y + M_z s_z\sigma_z - 3\sqrt{3}\chi\lambda_{\rm so}s_z\sigma_z, \tag{7}$$

where $\chi = 1$ for the valley $\mathbf{K}$ and -1 for the valley $\mathbf{K}'$. It is easy to see that the energy gap gets closed at $\mathbf{K}$ if $M_z = M_c \equiv 3\sqrt{3}\lambda_{\rm so}$, or at $\mathbf{K}'$ if $M_z = -M_c$ (a more accurate analysis finds out that the critical value of the exchange field is $M_c' = \lambda_{\rm so}(2+\eta)\sqrt{4-\eta^2}$).

Although the low-energy Hamiltonians above can capture the topological phase transition, it has higher symmetry than the full lattice Hamiltonian in Eq. (1), and the symmetry emergent from the leading-order approximation will force the intrinsic nonlinear Hall conductivity tensor (INLHCT) to vanish identically. To correctly obtain the INLHCT, we always adopt the full lattice Hamiltonian for calculations. It is noteworthy that if the lattice anisotropy is absent, the $\mathcal{C}_{3z}$ rotation symmetry will force all components of the INLHCT to vanish identically even for the full lattice Hamiltonian. When the lattice anisotropy is present, the remaining mirror symmetry about the xz plane forces the component $\chi^{\rm int}_{xyx}$ to vanish identically. Therefore, only the component $\chi^{\rm int}_{xyy}$ needs to be considered. To intuitively see that $\chi^{\rm int}_{xyx}$ is forced to vanish while $\chi^{\rm int}_{xyy}$ is not, we plot the distribution of the geometric quantity $\Lambda_{xyx}(\boldsymbol{k})$ and $\Lambda_{xyy}(\boldsymbol{k})$ in the Brillouin zone, as shown in Fig. 5. From Figs. 5(a) and 5(c), one sees that $\Lambda_{xyx}(\boldsymbol{k})$ is odd about k_y, leading to the vanishing of $\chi^{\rm int}_{xyx}$ after the integration over the Fermi surface. In contrast, Figs. 5(b) and 4(d) show that $\Lambda_{xyy}(\boldsymbol{k})$ is even about k_y, hence a nonzero $\Lambda_{xyy}(\boldsymbol{k})$ is permitted.

The numerical results for the INLHCT across the topological phase transition are shown in Fig. 6. Several prominent conclusions can be read from Fig. 6(a). First, the INLHCT does not change sign in the weakly-doped regime when the system transits from a quantum spin Hall insulator to a trivial insulator. This is quite different from the Berry-curvature-dipole NLHE which shows a sign change when an inversion

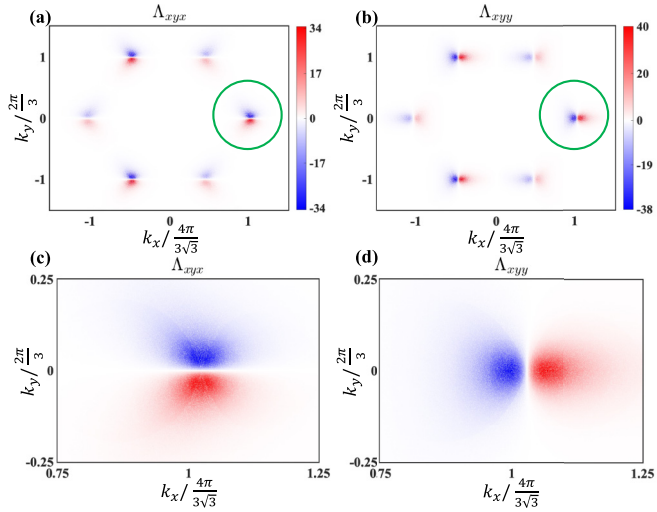

FIG. 5. The momentum-space distributions of the two geometric quantities, Λ_{xyx} and Λ_{xyy}, for the conduction bands. (c) and (d) are the zoom-in plot of the area enclosed by the green circle in (a) and (b), respectively. The parameters are given by $t_2 = 1$, $\eta = 1.1$, $\lambda_{\rm so} = 0.05$, $M_x = M_y = 0$ and $M_z = -0.2 + \lambda_{\rm so}(2+\eta)\sqrt{4-\eta^2}$.

asymmetric topological insulator transits to a trivial insulator [24,42,43]. The sign change of the Berry-curvature-dipole NLHE is simply due to the sign change of the Berry curvature across the topological phase transition. However, for topological phase transitions characterized by a Dirac Hamiltonian of the form in Eq. (7), it is easy to find that all components of the quantum metric tensor do not change sign when the Dirac mass changes sign. As the intrinsic NLHE is connected to the quantum metric, this explains why the INLHCT preserves its sign across this class of topological phase transitions. In a previous work, we have shown in the context of Hopf insulators that the INLHCT will change sign across a topological phase

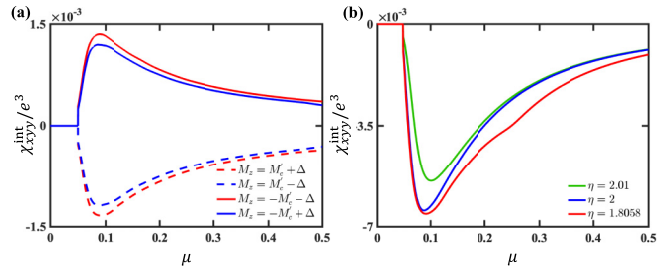

FIG. 6. The intrinsic NLHE before and after the topological phase transition from a quantum spin Hall insulator to a trivial insulator [(a)] and to a boundary-obstructed atomic insulator [(b)]. (a) The increase in the absolute value of M_z across the critical value, $M_c' = \lambda_{\rm so}(2+\eta)\sqrt{4-\eta^2}$, renders the system topologically trivial. The parameters are given by $\eta = 1.1$, $t_2 = 1$, $\lambda_{\rm so} = 0.05$ and $M_x = M_y = 0$. $\Delta = 0.05$ refers to half of the size of the bulk energy gap. (b) The quantum spin Hall insulator transits into a boundary-obstructed atomic insulator as η increases beyond 2. In order to evaluate the impact of the lattice anisotropy on the intrinsic NLHE, we maintain the gap around 0.1 by adjusting the strength of the lattice anisotropy. The parameters are given by $t_2 = 1$, $\lambda_{\rm so} = 0.05$, $M_x = M_y = 0$ and $M_z = 0.11$.

transition with the change of Hopf invariant [48]. Therein, the critical point is different from a Dirac point in many aspects, and it turns out that the quantum metric and Berry curvature are closely connected. These results suggest that whether the INLHCT changes sign or not is not a universal property, but depends on the type of the topological phase transition. A second conclusion can be obtained from Fig. 6(a) is that the INLHCT switches sign when the antiferromagnetic exchange field reverses its direction, which is expected as the effect is time-reversal-odd. Last but not the least, under the condition of the same bulk energy gap, the INLHCT can be enhanced by increasing the antiferromagnetic exchange field to cross the topological phase transition.

Next we consider the topological phase transition from a quantum spin Hall insulator to a boundary-obstructed atomic insulator driven by the lattice anisotropy. In Fig. 2, we have shown that, in the absence of spin-orbit coupling and antiferromagnetic exchange field, the two Dirac points will merge together at the **M** point when $\eta = 2$ or at the **Γ** point when $\eta = -2$ and form a critical semi-Dirac point. Since $\eta = -2$ means that the hopping constants t_1 and t_2 take opposite signs, which is not very realistic for a quantum material, below we will focus on the critical region at the neighborhood of $\eta = 2$, and explore the behavior of the INLHCT across the topological phase transition driven by lattice anisotropy.

As the spin-orbit coupling vanishes at **M**, a time-reversal invariant momentum, the mergence of Dirac points at this point when $\eta = 2$ indicates that the topological phase transition is associated with the close of energy gap at **M**. Therefore, we can do a low-energy expansion of the lattice Hamiltonian around this point. To capture the mergence of Dirac points, we keep the momentum up to the second order. The low-energy Hamiltonian is given by

$$\begin{aligned}\mathcal{H}_{\mathbf{M}}(\boldsymbol{q}) = t_2\left\{\left[\left(1-\frac{\eta}{2}\right)-\frac{3}{8}q_x^2\right]-\frac{\sqrt{3}(1+\eta)}{2}q_y\right\}s_0\sigma_x \\ -t_2\left\{\sqrt{3}\left[\left(1-\frac{\eta}{2}\right)-\frac{3}{8}q_x^2\right]+\frac{(1+\eta)}{2}q_y\right\}s_0\sigma_y \\ +(4\sqrt{3}\lambda_{\mathrm{so}}q_x+M_z)s_z\sigma_z. \qquad (8)\end{aligned}$$

Without the last term, the energy spectrum is given by

$$E_{\pm}(\boldsymbol{q}) = \pm t_2\sqrt{4\left[\left(1-\frac{\eta}{2}\right)-\frac{3}{8}q_x^2\right]^2+(1+\eta)^2q_y^2}, \qquad (9)$$

which displays the characteristic feature of a semi-Dirac point when $\eta = 2$, namely, the energy spectrum is quadratic in one direction and linear in the other direction [35,78,79]. Because the quantum metric and the density of states, two factors determining the conductivity tensor, are quite different between the Dirac point and the semi-Dirac point, different features are expected to show up in the INLHCT when the system undergoes this topological phase transition.

In Fig. 6(b), we show the INLHCT under different strength of lattice anisotropy and fixed spin-orbit coupling and exchange field. Fixing the band gap by adjusting the strength of lattice anisotropy, we find that the INLHCT still does not change sign across the topological phase transition. However, the INLHCT is considerably enhanced near this topological phase transition even for a weak exchange field. The result suggests that the lattice anisotropy can be applied as an effective factor to engineer strong intrinsic NLHE.

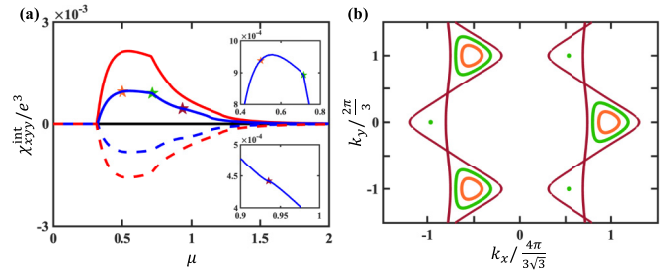

FIG. 7. (a) $\chi^{\mathrm{int}}_{xyy}$ as a function of the chemical potential μ; (b) The corresponding evolution of Fermi surface for the blue solid line in (a). In (a), the red solid line, blue solid line, black solid line, blue dashed line, and red dashed line refer to cases with $t_2 = 1$, $\eta = 0.8$, 0.9, 1, 1.1 and 1.2, respectively. In (b), Fermi surfaces corresponding to $\mu = 0.5$, 0.718 and 0.935 are plotted in orange, green and dark red, respectively. Shared parameters: $t_2 = 1$, $\lambda_{\mathrm{so}} = 0.1$, $M_x = M_y = 0$ and $M_z = 0.2$.

IV. DETECTING BASIC MATERIAL PROPERTIES VIA INTRINSIC NLHE

A. Manifestation of Lifshitz transitions

The band structure of the honeycomb-lattice model is interesting not only for its nontrivial topology, but also for properties like valley polarization and the existence of van Hove singularities carrying divergent density of states [80]. By adjusting the Fermi level, both the valley polarization and the van Hove singularities will manifest through the Lifshitz transitions, the change of Fermi surfaces in topology [81].

In Fig. 7, we show the evolution of INLHCT and Fermi surface with respect to the chemical potential on the left and right panel, respectively. Three interesting features can be read from Fig. 7(a). The first one is that the INLHCT vanishes identically when $\eta = 1$, revealing that the breaking of the $\mathcal{C}_{3z}$ rotation symmetry is necessary for observing this effect. The second one is the sign change of the INLHCT when η goes across 1, indicating that applying tensile or compressive strain can tune both the magnitude and the direction of the nonlinear Hall current. The second one is the existence of kinks on the INLHCT curves, as highlighted by the two stars in green and dark red on the blue solid curve. By plotting the Fermi surfaces under the chemical potential corresponding to the three stars of different colors, we find that the kink highlighted by the green star corresponds to a Lifshitz transition with a new Fermi surface emerging at the $\mathbf{K}'$ valley [the small green dots in Fig. 7(b)]. This result suggests that the intrinsic NLHE is valley-polarized for chemical potential below this value [there is only one Fermi surface at the **K** valley, see the triangle-shaped orange ring in Fig. 7(b)]. For the kink highlighted by the dark red star, it corresponds to a Lifshitz transition with the touching of the two Fermi surfaces centered at **K** and $\mathbf{K}'$ valleys (see the Fermi surfaces in dark red). The touching point is a saddle point, which corresponds to a van Hove singularity. The results above suggest that the intrinsic NLHE, as a Fermi-surface property depending on the density

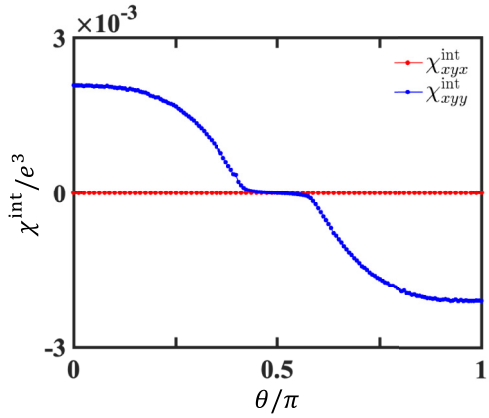

FIG. 8. $\chi^{\rm int}_{xyy}$ and $\chi^{\rm int}_{xyx}$ as a function of the polar angle θ. The parameters are $\eta = 0.8$, $t_2 = 1$, $\lambda_{\rm so} = 0.1$, $\mu = 0.5$ and the magnitude of the exchange field is fixed to 0.2, i.e., $\sqrt{M_x^2 + M_y^2 + M_z^2} = 0.2$.

of states, can detect the Lifshitz transitions which is associated with a dramatic change of Fermi surface and the presence of nonanalyticity in the density of states.

B. Detecting the Néel vector

Now we move to explore the dependence of INLHTC on the direction of the Néel vector. Without the spin-orbit coupling, the Hamiltonian has spin-rotation symmetry and the intrinsic NLHE does not depend on the direction of the Néel vector. In other words, the intrinsic NLHE cannot reflect the Néel vector if there is no spin-orbit coupling to break the spin rotation symmetry. For the spin-orbit coupling considered, the full spin rotation symmetry is broken down to a fixed-axis rotation symmetry, i.e., the system is invariant only when the spin is rotated about the z axis. Therefore, if we view the Néel vector in the spherical coordinate system, the INLHTC is expected to depend on the polar angle but not on the azimuthal angle of the Néel vector.

By fixing the value of all parameters and only changing the direction of the Néel vector, we calculate the evolution of the INLHTC with respect to the polar angle of the Néel vector and present the numerical result in Fig. 8. The result clearly shows an angle dependence, suggesting the capability of the intrinsic NLHE to detect the information of the Néel vector. In Fig. 8, another notable feature is that the INLHTC vanishes when the polar angle θ equals $\pi/2$, which corresponds to that the Néel vector lies in the xy plane. The vanishing of INLHTC is due to the emergence of an effective spinless time-reversal symmetry at this specific polar angle. To be specific, at $\theta = \pi/2$, we find that there exists an operator of the form $\tilde{\mathcal{T}} = s_x\sigma_0\mathcal{K}$, satisfying $\tilde{\mathcal{T}}\mathcal{H}(\boldsymbol{k})\mathcal{T}^{-1} = \mathcal{H}(-\boldsymbol{k})$ and $\tilde{\mathcal{T}}^2 = 1$. Physically, this effective time-reversal symmetry is a combinational symmetry composed of the mirror operation about the xy plane and the spinful time-reversal operation, i.e., $\tilde{\mathcal{T}} = \mathcal{M}_z\mathcal{T}$. While the mirror symmetry $\mathcal{M}_z$ and the spinful time-reversal symmetry $\mathcal{T}$ are independently broken by the in-plane exchange field, their combination remains intact for this special case. As mentioned, the intrinsic NLHE is a time-reversal-odd effect, the emergence of this time-reversal symmetry thereby forces it to vanish.

V. DISCUSSIONS AND CONCLUSIONS

We have explored the intrinsic NLHE in 2D honeycomb antiferromagnets with $\mathcal{PT}$ symmetry. As a class of systems supporting a number of interesting topological phases, we investigated the behavior of the intrinsic NLHE across two types of topological phase transitions. We found that, unlike the Berry-curvature-dipole NLHE, the intrinsic NLHE does not switch direction when the system undergoes a Dirac-type topological phase transition, suggesting that the intrinsic NLHE cannot be applied to detect such topological phase transitions. Nevertheless, the intrinsic NLHE could become prominent near these topological phase transitions, owing to that the quantum metric is inversely proportional to the band gap. We found that the lattice anisotropy breaking the $\mathcal{C}_{3z}$ rotation symmetry is not only necessary for the presence of intrinsic NLHE, but also serves as an effective factor to tune its magnitude and direction. As a Fermi-surface property, we found that the intrinsic NLHE can manifest Lifshitz transitions. Furthermore, we found that the existence of spin-orbit coupling to lift the spin-rotation symmetry is crucial for the intrinsic NLHE to detect the Néel vector. Our findings show that the 2D honeycomb antiferromagnets could serve as fertile ground to study the intrinsic NLHE.

ACKNOWLEDGMENTS

This work is supported by the National Natural Science Foundation of China (Grant No. 12174455), the Natural Science Foundation of Guangdong Province (Grant No. 2021B1515020026), and the Guangdong Basic and Applied Basic Research Foundation (Grant No. 2023B1515040023).

[1] J. P. Provost and G. Vallee, Riemannian structure on manifolds of quantum states, Commun. Math. Phys. **76**, 289 (1980).
[2] D. J. Thouless, M. Kohmoto, M. P. Nightingale, and M. den Nijs, Quantized Hall conductance in a two-dimensional periodic potential, Phys. Rev. Lett. **49**, 405 (1982).
[3] C.-Z. Chang, C.-X. Liu, and A. H. MacDonald, Colloquium: Quantum anomalous Hall effect, Rev. Mod. Phys. **95**, 011002 (2023).
[4] N. Nagaosa, J. Sinova, S. Onoda, A. H. MacDonald, and N. P. Ong, Anomalous Hall effect, Rev. Mod. Phys. **82**, 1539 (2010).
[5] K.-Y. Yang, Y.-M. Lu, and Y. Ran, Quantum Hall effects in a Weyl semimetal: Possible application in pyrochlore iridates, Phys. Rev. B **84**, 075129 (2011).
[6] D. Xiao, M.-C. Chang, and Q. Niu, Berry phase effects on electronic properties, Rev. Mod. Phys. **82**, 1959 (2010).
[7] S. Peotta and P. Törmä, Superfluidity in topologically nontrivial flat bands, Nat. Commun. **6**, 8944 (2015).
[8] A. Julku, S. Peotta, T. I. Vanhala, D.-H. Kim, and P. Törmä, Geometric origin of superfluidity in the Lieb-lattice flat band, Phys. Rev. Lett. **117**, 045303 (2016).

[9] L. Liang, T. I. Vanhala, S. Peotta, T. Siro, A. Harju, and P. Törmä, Band geometry, berry curvature, and superfluid weight, Phys. Rev. B **95**, 024515 (2017).

[10] X. Hu, T. Hyart, D. I. Pikulin, and E. Rossi, Geometric and conventional contribution to the superfluid weight in twisted bilayer graphene, Phys. Rev. Lett. **123**, 237002 (2019).

[11] F. Xie, Z. Song, B. Lian, and B. A. Bernevig, Topology-bounded superfluid weight in twisted bilayer graphene, Phys. Rev. Lett. **124**, 167002 (2020).

[12] K.-E. Huhtinen, J. Herzog-Arbeitman, A. Chew, B. A. Bernevig, and P. Törmä, Revisiting flat band superconductivity: Dependence on minimal quantum metric and band touchings, Phys. Rev. B **106**, 014518 (2022).

[13] W. Chen and W. Huang, Quantum-geometry-induced intrinsic optical anomaly in multiorbital superconductors, Phys. Rev. Res. **3**, L042018 (2021).

[14] J. Ahn, G.-Y. Guo, N. Nagaosa, and A. Vishwanath, Riemannian geometry of resonant optical responses, Nat. Phys. **18**, 290 (2022).

[15] Y. Onishi and L. Fu, Fundamental bound on topological gap, Phys. Rev. X **14**, 011052 (2024).

[16] P. Törmä, Essay: Where can quantum geometry lead us? Phys. Rev. Lett. **131**, 240001 (2023).

[17] J. E. Moore and J. Orenstein, Confinement-induced berry phase and helicity-dependent photocurrents, Phys. Rev. Lett. **105**, 026805 (2010).

[18] Y. Gao, S. A. Yang, and Q. Niu, Field induced positional shift of bloch electrons and its dynamical implications, Phys. Rev. Lett. **112**, 166601 (2014).

[19] I. Sodemann and L. Fu, Quantum nonlinear Hall effect induced by berry curvature dipole in time-reversal invariant materials, Phys. Rev. Lett. **115**, 216806 (2015).

[20] S.-Y. Xu, Q. Ma, H. Shen, V. Fatemi, S. Wu, T.-R. Chang, G. Chang, A. M. M. Valdivia, C.-K. Chan, Q. D. Gibson, J. Zhou, Z. Liu, K. Watanabe, T. Taniguchi, H. Lin, R. J. Cava, L. Fu, N. Gedik, and P. Jarillo-Herrero, Electrically switchable berry curvature dipole in the monolayer topological insulator WTe_2, Nat. Phys. **14**, 900 (2018).

[21] Y. Zhang, Y. Sun, and B. Yan, Berry curvature dipole in Weyl semimetal materials: An *ab initio* study, Phys. Rev. B **97**, 041101(R) (2018).

[22] J.-S. You, S. Fang, S.-Y. Xu, E. Kaxiras, and T. Low, Berry curvature dipole current in the transition metal dichalcogenides family, Phys. Rev. B **98**, 121109(R) (2018).

[23] Y. Zhang, J. van den Brink, C. Felser, and B. Yan, Electrically tuneable nonlinear anomalous Hall effect in two-dimensional transition-metal dichalcogenides WTe_2 and $MoTe_2$, 2D Mater. **5**, 044001 (2018).

[24] Z. Z. Du, C. M. Wang, H.-Z. Lu, and X. C. Xie, Band signatures for strong nonlinear Hall effect in bilayer WTe_2, Phys. Rev. Lett. **121**, 266601 (2018).

[25] J. I. Facio, D. Efremov, K. Koepernik, J.-S. You, I. Sodemann, and J. van den Brink, Strongly enhanced Berry dipole at topological phase transitions in BiTeI, Phys. Rev. Lett. **121**, 246403 (2018).

[26] Q. Ma, S.-Y. Xu, H. Shen, D. MacNeill, V. Fatemi, T.-R. Chang, A. M. Mier Valdivia, S. Wu, Z. Du, C.-H. Hsu, S. Fang, Q. D. Gibson, K. Watanabe, T. Taniguchi, R. J. Cava, E. Kaxiras, H.-Z. Lu, H. Lin, L. Fu, N. Gedik *et al.*, Observation of the nonlinear hall effect under time-reversal-symmetric conditions, Nature (London) **565**, 337 (2019).

[27] K. Kang, T. Li, E. Sohn, J. Shan, and K. F. Mak, Nonlinear anomalous Hall effect in few-layer WTe_2, Nat. Mater. **18**, 324 (2019).

[28] R. Battilomo, N. Scopigno, and C. Ortix, Berry curvature dipole in strained graphene: A Fermi surface warping effect, Phys. Rev. Lett. **123**, 196403 (2019).

[29] H. Wang and X. Qian, Ferroelectric nonlinear anomalous Hall effect in few-layer WTe_2, npj Comput. Mater. **5**, 119 (2019).

[30] C. Xiao, Z. Z. Du, and Q. Niu, Theory of nonlinear Hall effects: Modified semiclassics from quantum kinetics, Phys. Rev. B **100**, 165422 (2019).

[31] H. Rostami and V. Juričić, Probing quantum criticality using nonlinear Hall effect in a metallic Dirac system, Phys. Rev. Res. **2**, 013069 (2020).

[32] S. Singh, J. Kim, K. M. Rabe, and D. Vanderbilt, Engineering Weyl phases and nonlinear Hall effects in t_d-$MoTe_2$, Phys. Rev. Lett. **125**, 046402 (2020).

[33] C. Zeng, S. Nandy, and S. Tewari, Nonlinear transport in Weyl semimetals induced by berry curvature dipole, Phys. Rev. B **103**, 245119 (2021).

[34] P. A. Pantaleón, T. Low, and F. Guinea, Tunable large Berry dipole in strained twisted bilayer graphene, Phys. Rev. B **103**, 205403 (2021).

[35] S. S. Samal, S. Nandy, and K. Saha, Nonlinear transport without spin-orbit coupling or warping in two-dimensional Dirac semimetals, Phys. Rev. B **103**, L201202 (2021).

[36] D. Kumar, C.-H. Hsu, R. Sharma, T.-R. Chang, P. Yu, J. Wang, G. Eda, G. Liang, and H. Yang, Room-temperature nonlinear hall effect and wireless radiofrequency rectification in Weyl semimetal $TaIrTe_4$, Nat. Nanotechnol. **16**, 421 (2021).

[37] Z.-S. Liao, H.-H. Zhang, and Z. Yan, Nonlinear Hall effect in two-dimensional class-ai metals, Phys. Rev. B **103**, 235151 (2021).

[38] C.-P. Zhang, J. Xiao, B. T. Zhou, J.-X. Hu, Y.-M. Xie, B. Yan, and K. T. Law, Giant nonlinear Hall effect in strained twisted bilayer graphene, Phys. Rev. B **106**, L041111 (2022).

[39] A. Bandyopadhyay, N. B. Joseph, and A. Narayan, Electrically switchable giant Berry curvature dipole in silicene, germanene and stanene, 2D Mater. **9**, 035013 (2022).

[40] S. Roy and A. Narayan, Non-linear Hall effect in multi-Weyl semimetals, J. Phys.: Condens. Matter **34**, 385301 (2022).

[41] M. S. Okyay, S. A. Sato, K. W. Kim, B. Yan, H. Jin, and N. Park, Second harmonic Hall responses of insulators as a probe of Berry curvature dipole, Commun. Phys. **5**, 303 (2022).

[42] S. Sinha, P. C. Adak, A. Chakraborty, K. Das, K. Debnath, L. D. V. Sangani, K. Watanabe, T. Taniguchi, U. V. Waghmare, A. Agarwal, and M. M. Deshmukh, Berry curvature dipole senses topological transition in a moiré superlattice, Nat. Phys. **18**, 765 (2022).

[43] A. Chakraborty, K. Das, S. Sinha, P. C. Adak, M. M. Deshmukh, and A. Agarwal, Nonlinear anomalous Hall effects probe topological phase-transitions in twisted double bilayer graphene, 2D Mater. **9**, 045020 (2022).

[44] K. Das, S. Lahiri, R. B. Atencia, D. Culcer, and A. Agarwal, Intrinsic nonlinear conductivities induced by the quantum metric, Phys. Rev. B **108**, L201405 (2023).

[45] J. Wang, H. Zeng, W. Duan, and H. Huang, Intrinsic nonlinear Hall detection of the Néel vector for two-dimensional antiferromagnetic spintronics, Phys. Rev. Lett. **131**, 056401 (2023).

[46] C.-P. Zhang, X.-J. Gao, Y.-M. Xie, H. C. Po, and K. T. Law, Higher-order nonlinear anomalous Hall effects induced by Berry curvature multipoles, Phys. Rev. B **107**, 115142 (2023).

[47] R. B. Atencia, D. Xiao, and D. Culcer, Disorder in the nonlinear anomalous Hall effect of $\mathcal{PT}$-symmetric Dirac fermions, Phys. Rev. B **108**, L201115 (2023).

[48] Z.-Y. Zhuang and Z. Yan, Extrinsic and intrinsic nonlinear Hall effects across Berry-dipole transitions, Phys. Rev. B **107**, L161102 (2023).

[49] M. Huang, Z. Wu, X. Zhang, X. Feng, Z. Zhou, S. Wang, Y. Chen, C. Cheng, K. Sun, Z. Y. Meng, and N. Wang, Intrinsic nonlinear hall effect and gate-switchable Berry curvature sliding in twisted bilayer graphene, Phys. Rev. Lett. **131**, 066301 (2023).

[50] S. Saha and A. Narayan, Nonlinear Hall effect in Rashba systems with hexagonal warping, J. Phys.: Condens. Matter **35**, 485301 (2023).

[51] A. Kirikoshi and S. Hayami, Microscopic mechanism for intrinsic nonlinear anomalous Hall conductivity in noncollinear antiferromagnetic metals, Phys. Rev. B **107**, 155109 (2023).

[52] B. Hetényi and P. Lévay, Fluctuations, uncertainty relations, and the geometry of quantum state manifolds, Phys. Rev. A **108**, 032218 (2023).

[53] Y.-X. Huang, C. Xiao, S. A. Yang, and X. Li, Scaling law for time-reversal-odd nonlinear transport, arXiv:2311.01219.

[54] D. Kaplan, T. Holder, and B. Yan, Unification of nonlinear anomalous Hall effect and nonreciprocal magnetoresistance in metals by the quantum geometry, Phys. Rev. Lett. **132**, 026301 (2024).

[55] D. Mandal, S. Sarkar, K. Das, and A. Agarwal, Quantum geometry induced third order nonlinear transport responses, arXiv:2310.19092.

[56] Q. Ma, A. G. Grushin, and K. S. Burch, Topology and geometry under the nonlinear electromagnetic spotlight, Nat. Mater. **20**, 1601 (2021).

[57] Z. Z. Du, H.-Z. Lu, and X. C. Xie, Nonlinear Hall effects, Nat. Rev. Phys. **3**, 744 (2021).

[58] C. Ortix, Nonlinear Hall effect with time-reversal symmetry: Theory and material realizations, Adv. Quantum Technol. **4**, 2100056 (2021).

[59] A. Bandyopadhyay, N. Benno Joseph, and A. Narayan, Nonlinear Hall effects: Mechanisms and materials, Mater. Today Electro. **8**, 100101 (2024).

[60] H. Liu, J. Zhao, Y.-X. Huang, W. Wu, X.-L. Sheng, C. Xiao, and S. A. Yang, Intrinsic second-order anomalous Hall effect and its application in compensated antiferromagnets, Phys. Rev. Lett. **127**, 277202 (2021).

[61] C. Wang, Y. Gao, and D. Xiao, Intrinsic nonlinear Hall effect in antiferromagnetic tetragonal cumnas, Phys. Rev. Lett. **127**, 277201 (2021).

[62] L. Šmejkal, J. Železný, J. Sinova, and T. Jungwirth, Electric control of Dirac quasiparticles by spin-orbit torque in an antiferromagnet, Phys. Rev. Lett. **118**, 106402 (2017).

[63] Y. Xu, Z. Song, Z. Wang, H. Weng, and X. Dai, Higher-order topology of the axion insulator $EuIn_2As_2$, Phys. Rev. Lett. **122**, 256402 (2019).

[64] A. Gao, Y.-F. Liu, J.-X. Qiu, B. Ghosh, T. V. Trevisan, Y. Onishi, C. Hu, T. Qian, H.-J. Tien, S.-W. Chen, M. Huang, D. Bérubé, H. Li, C. Tzschaschel, T. Dinh, Z. Sun, S.-C. Ho, S.-W. Lien, B. Singh, K. Watanabe *et al.*, Quantum metric nonlinear Hall effect in a topological antiferromagnetic heterostructure, Science **381**, 181 (2023).

[65] N. Wang, D. Kaplan, Z. Zhang, T. Holder, N. Cao, A. Wang, X. Zhou, F. Zhou, Z. Jiang, C. Zhang, S. Ru, H. Cai, K. Watanabe, T. Taniguchi, B. Yan, and W. Gao, Quantum-metric-induced nonlinear transport in a topological antiferromagnet, Nature (London) **621**, 487 (2023).

[66] C. Niu, J. P. Hanke, P.-M. Buhl, G. Bihlmayer, D. Wortmann, S. Blügel, and Y. Mokrousov, Quantum spin Hall effect and topological phase transitions in honeycomb antiferromagnets, arXiv:1705.07035.

[67] X. Zou, H. Ma, R. Li, Y. Dai, B. Huang, and C. Niu, Gate-mediated transition between antiferromagnetic topological and chern insulators in honeycomb $X_3MnN_3(x = \mathrm{Sr}, \mathrm{Ba})$, Phys. Rev. B **106**, 075144 (2022).

[68] B. Li, W. Sun, X. Zou, X. Li, B. Huang, Y. Dai, and C. Niu, Switchable quantum anomalous and spin Hall effects inhoneycomb magnet $EuCd_2As_2$, New J. Phys. **24**, 053038 (2022).

[69] C. L. Kane and E. J. Mele, Quantum spin Hall effect in graphene, Phys. Rev. Lett. **95**, 226801 (2005).

[70] C. L. Kane and E. J. Mele, Z_2 topological order and the quantum spin Hall effect, Phys. Rev. Lett. **95**, 146802 (2005).

[71] A. H. Castro Neto, F. Guinea, N. M. R. Peres, K. S. Novoselov, and A. K. Geim, The electronic properties of graphene, Rev. Mod. Phys. **81**, 109 (2009).

[72] V. M. Pereira, A. H. Castro Neto, and N. M. R. Peres, Tight-binding approach to uniaxial strain in graphene, Phys. Rev. B **80**, 045401 (2009).

[73] B. Wang, X. Zhou, H. Lin, and A. Bansil, Higher-order topological insulator phase in a modified Haldane model, Phys. Rev. B **104**, L121108 (2021).

[74] S. Lahiri and S. Basu, Wannier charge center, spin resolved bulk polarization and corner modes in a strained quantum spin Hall insulator, Phys. Rev. B **109**, 115424 (2024).

[75] D. N. Sheng, Z. Y. Weng, L. Sheng, and F. D. M. Haldane, Quantum spin-Hall effect and topologically invariant Chern numbers, Phys. Rev. Lett. **97**, 036808 (2006).

[76] J. C. Y. Teo, L. Fu, and C. L. Kane, Surface states and topological invariants in three-dimensional topological insulators: Application to $Bi_{1-x}Sb_x$, Phys. Rev. B **78**, 045426 (2008).

[77] C.-M. Miao, Y.-H. Wan, Q.-F. Sun, and Y.-T. Zhang, Engineering topologically protected zero-dimensional interface end states in antiferromagnetic heterojunction graphene nanoflakes, Phys. Rev. B **108**, 075401 (2023).

[78] P. Dietl, F. Piéchon, and G. Montambaux, New magnetic field dependence of Landau levels in a graphenelike structure, Phys. Rev. Lett. **100**, 236405 (2008).

[79] S. Banerjee, R. R. P. Singh, V. Pardo, and W. E. Pickett, Tight-binding modeling and low-energy behavior of the semi-dirac point, Phys. Rev. Lett. **103**, 016402 (2009).

[80] L. Van Hove, The occurrence of singularities in the elastic frequency distribution of a crystal, Phys. Rev. **89**, 1189 (1953).

[81] G. E. Volovik, Topological Lifshitz transitions, Low Temp. Phys. **43**, 47 (2017).